IEEE Robotics and Automation Letters (RA-L) paper, presented at ICRA 2026, Vienna, Austria. Cite as RA-L paper.

Online Velocity Estimation of a Robotic Fish Using Artificial Lateral Line System With Velocity-Decoupling Sensing Ability

Jiarui He, Yan Zhou, Chengqian Zhang, Huangzhe Dai, Daofan Tang, Chengfeng Pan, and Peng Zhao, *Member, IEEE*

***Abstract*—The robotic fish has attracted widespread research interest over the past few decades, due to its outstanding agility and environmental friendliness. And the sensing ability of underwater environments is crucial for the robotic fish to accomplish various underwater tasks. Inspired by the lateral line of real fish, many types of artificial lateral line (ALL) sensors have been proposed, including pressure-based sensors and deformation-based sensors. However, currently these types of ALL sensors mounted on robotic fish are susceptible to the interference from robotic fish's self-motions such as yaw motion and pitch motion, as well as the unavoidable vortices around the robotic fish. To address the above issues, a deformation-based magnetic ALL sensor capable of flow velocity-decoupling sensing is proposed, which can be used to measure the swimming speed of the robotic fish while suppressing the aforementioned noise. Besides, an ALL array is designed and mounted on both sides of a robotic fish, enabling the measurement of its swimming speed under both rectilinear and turning motion, with a mean absolute error (MAE) of 0.0153 m/s and 0.0125 m/s, respectively. Based on this, the ALL array is applied for trajectory estimation of the robotic fish, and the MAE of trajectory estimation under rectilinear and turning motion is 0.0600 m and 0.0730 m, respectively.**

Received 26 April 2025; accepted 7 August 2025. Date of publication 20 August 2025; date of current version 29 August 2025. This letter was recommended for publication by Associate Editor P. Manoonpong and Editor C. Laschi upon evaluation of the reviewers' comments. This work was supported in part by the National Natural Science Foundation of China under Grant 52205424 and Grant 524B2062, in part by the State Key Laboratory of Materials Processing and Die & Mould Technology, Huazhong University of Science and Technology under Grant P2024-010, in part by the China National Postdoctoral Program for Innovative Talents under Grant BX20240321, and in part by Zhejiang Provincial Teams of Leading Talents in Innovation and Entrepreneurship under Grant 2024R01002. *(Corresponding authors: Chengqian Zhang; Peng Zhao.)*

Jiarui He, Huangzhe Dai, Daofan Tang, Chengfeng Pan, and Peng Zhao are with the State Key Laboratory of Fluid Power and Mechatronic Systems, School of Mechanical Engineering, Zhejiang University, Hangzhou 310058, China, and also with the Zhejiang Key Laboratory of Additive Manufacturing Technology and Equipment, School of Mechanical Engineering, Zhejiang University, Hangzhou 310058, China (e-mail: hejiarui@zju.edu.cn; 22125067@zju.edu.cn; 21925024@zju.edu.cn; cfpan@zju.edu.cn; pengzhao@zju.edu.cn).

Yan Zhou is with the College of Design and Engineering, National University of Singapore, Singapore 119077 (e-mail: e1546952@u.nus.edu).

Chengqian Zhang is with the State Key Laboratory of Fluid Power and Mechatronic Systems, School of Mechanical Engineering, Zhejiang University, Hangzhou 310058, China, also with the Zhejiang Key Laboratory of Additive Manufacturing Technology and Equipment, School of Mechanical Engineering, Zhejiang University, Hangzhou 310058, China, and also with the State Key Laboratory of Materials Processing and Die & Mould Technology, Huazhong University of Science and Technology, Wuhan 430074, China (e-mail: zhangcq@zju.edu.cn).

This article has supplementary downloadable material available at https://doi.org/10.1109/LRA.2025.3601030, provided by the authors.

Digital Object Identifier 10.1109/LRA.2025.3601030

***Index Terms*—Biologically-inspired robots, marine robotics, soft sensors and actuators.**

I. Introduction

THE oceans cover more than 70% of the Earth's surface and provide a wealth of resources for humankind [1], [2]. In order to make good use of marine resources, it is necessary to design and manufacture underwater vehicles that are easy to operate, highly efficient, and possess high autonomy to accomplish specific underwater tasks [3]. Among them, significant progress has been made in the research of robotic fish, due to their outstanding agility and environmental friendliness [4], [5], [6]. Thus, robotic fish have been applied in many underwater fields. Specifically, Daniela's group developed a soft robotic fish capable of swimming in a three-dimensional marine environment, and it can perform underwater exploration through acoustic control [7]. Fang's group developed a novel bioinspired robotic dolphin with excellent environmental adaptability and safety, capable of performing water quality monitoring [8]. Xie's group developed a fin-actuated robotic fish that can achieve online state estimation such as velocity and trajectory [9]. However, due to the complexity of the underwater environment, the flow velocity sensing capability of robotic fish has become an urgent issue to address, which can help robotic fish adapt to the environment and perform multiple underwater tasks [10].

The lateral line system is a unique sensory organ in fish and amphibians, playing an essential role in activities such as hunting, predator avoidance, group travel, and reproduction [11]. For example, the Mexican blind cavefish uses a lateral line system for underwater navigation [12]. This has inspired researchers to mimic the lateral line system of real fish and develop a series of artificial lateral line (ALL) sensors. Currently, the fluid structure coupling ALL sensors can be divided into two types: pressure-based ALL sensors and deformation-based ALL sensors [13], [10]. The pressure-based ALL sensors sense the flow field information by measuring the water pressure [14], [15], [16]. For example, Xie's group proposed an ALL system composed of nine pressure sensors and developed a nonlinear prediction model to detect the swimming speed of a robotic fish [14]. However, most pressure-based ALL sensors are incapable of capturing point-wise velocity on the robotic fish body. Moreover, as they rely on sensing subtle pressure variations induced by flow velocity under absolute water pressure, the pressure-based ALL sensors are sensitive to environmental noise [13]. Deformation-based ALL sensors operate by detecting flow-induced deformations of their

IEEE Robotics and Automation Letters (RA-L) paper, presented at ICRA 2026, Vienna, Austria. Cite as RA-L paper.

sensitive elements, with variations in the output signals used to infer flow field characteristics [13], [17], [18]. For example, Tan's group proposed an ALL sensor based on a L-shaped cantilever structure, capable of measuring the swimming speed of robotic fish by detecting cantilever deformation induced by water impact. Furthermore, they developed a kinematic fusion approach for the ALL sensor array to estimate the velocity vector of the robotic fish [13]. Although deformation-based ALL sensors can achieve pointwise velocity measurements, the robotic fish's self-motions such as yaw motion and pitch motion, as well as the unavoidable vortices present around the ALL sensors, can cause the deformation of the sensitive element in the non-velocity direction, thus resulting in velocity measurement errors. Therefore, developing an ALL sensor that can realize the measurement of velocity in a specified direction, thus suppressing the influence of non-velocity direction noise, remains a significant and challenging task.

To address the aforementioned issues, this work developed a deformation-based ALL sensor capable of velocity-decoupling measurements and suppressing errors caused by both the robotic fish's self-motions and the vortices near the sensors. We also designed an ALL array that enables real-time acquisition of the robotic fish's velocity magnitude, and furthermore achieving trajectory estimation of the robotic fish. The main contributions of the letter are as follows:

1) A magnetic ALL flow sensor is proposed, which has three-dimensional flow velocity-decoupling sensing capability, allowing it to remain unaffected by the self-motion noise of the robotic fish as well as the vortices interference in non-velocity directions.
2) An ALL array was designed and installed on a robotic fish, enabling the robotic fish to perceive its velocity magnitude at multiple locations. By selecting appropriate installation locations and fusing the data from the ALL array, the estimation error can be effectively reduced.
3) Based on the estimation of the robotic fish's swimming velocity, the ALL sensor is applied for the robotic fish's trajectory esitimation under both rectilinear and turning motion.

II. Development of the Robotic Fish

A. Robot Prototype Design

Lateral line is a sensory system that is composed of numerous neuromast units, usually spreading over the head and trunk of fish [19]. Fig. 1(a) shows the basic unit of lateral line, including cupula, colloid and hair cells. When water flows through the Cupula, the deformation is transmitted to the bundle of the neuromast by the colloid, which in turn stimulates the hair cells below to produce nerve impluses, thus allowing the fish to sense the flow direction and velocity [20]. Mimicking the structure of lateral line, a magnetic ALL flow sensor is proposed, whose structure consists of a magnetic film, a deformed layer and a Hall sensor. The specifics of the sensor will be discussed in later chapters.

In order to detect the flow field information around the robotic fish, an ALL array is placed inside and on the surface of the robotic fish. Fig. 1(b) and (c) show the overview and detailed configurations of the developed robotic fish. It mainly consists of a body part, a wire-driven tail part and a caudal fin for bionic swimming. And the size of the robotic fish is 492 × 106 × 158 mm. The electronic system is composed of a battery compartment, an engine compartment, a control compartment and a sense compartment. The tail part has four vertebrae, and a pair of wires passes through the first three vertebrae and fastens at the fourth one. The other end of the wires is mounted on the reel of a waterproof servomotor, which drives the reel and swings the tail, providing the fish with different swimming motions.

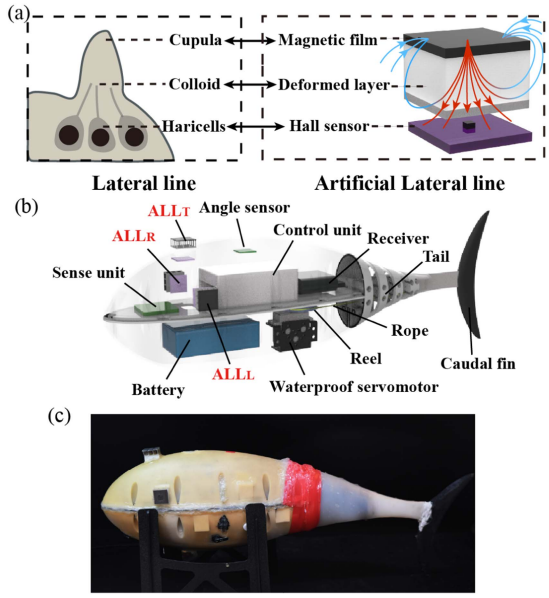

Fig. 1. Lateral line morphology and the prototype of robotic fish. (a) The fish's lateral line and its inspired artificial lateral line structure. (b) The mechanical structure and electronics of the robotic fish. (c) Prototype of the robotic fish.

The ALL array contains three ALL sensors in total. Among them, two sensors are placed on both sides of the fish and one on the head, each noted as ALL_L, ALL_R and ALL_T, respectively, and are used to measure the velocity of the left, right and center sides of the fish. Another angle sensor is placed inside the middle of the robotic fish to detect the swimming direction by measuring the environmental magnetic field. The data collected by the ALL system and angle sensor is transmitted to a circuit board via the I2C bus, while another circuit board used to control the robotic fish's swimming motion is connected with a receiver, which can transmit commands from a wireless controller.

B. Structure of the ALL Sensor

Inspired by fish's lateral line, an ALL flow sensor with 3D magnetic-based decoupling perception capability is proposed. The basic structure of the sensor is like a sandwich, consisting a magnetic film, an elastic deformable supporting layer and a 3D Hall sensor, as shown in Fig. 2(a). The top layer is the magnetic film encased in silicone elastomer, which is the component that generates the magnetic field. To ensure that the size of the ALL sensor matches the overall dimensions of the robotic fish and that the magnetic field generated is strong enough to be sensed by the Hall sensor [21], the size of the magnetic film is 20 mm × 20 mm × 1 mm. The middle layer is a 4 × 4 elastic array made of silicone with a thickness of 10 mm, which supports the magnetic film and accommodates appropriate deformation induced by water flow. The bottom layer, installed inside the robotic fish, is a 3D Hall sensor (MLX90393, 20.4 mm × 20.4 mm × 5 mm) that measures

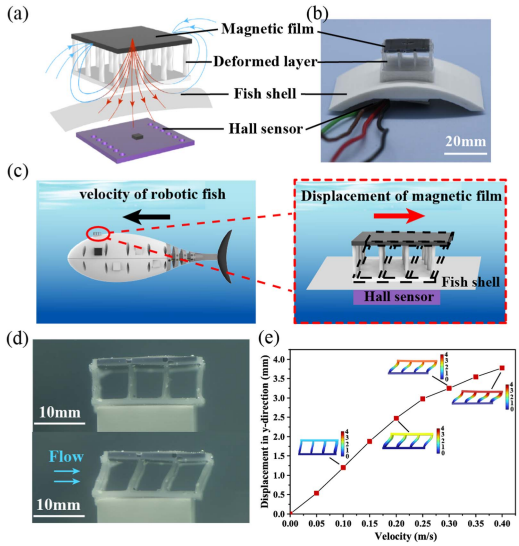

Fig. 2. Structure and working principle of the ALL. (a) Illustration of the structures of the ALL sensor. (b) Actual prototype of the ALL sensor. (c) The ALL sensor mounted on the robotic fish. (d) Displacement of the magnetic film as water flows over. (e) Simulation results of the magnetic film displacement and flow velocity (in COMSOL).

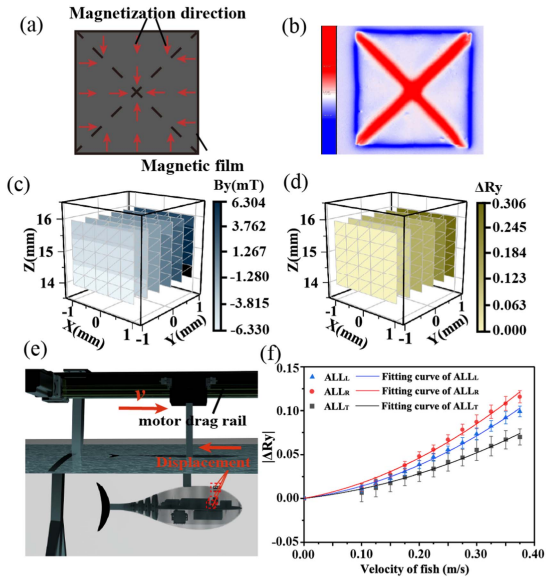

Fig. 3. Performance of the ALL. (a) Diagram of the film centripetal magnetization. (b) Magnetic field distribution of the magnetic film captured by a magneto-optic camera. (c) Magnetic field component B_y under the triaxial displacement of the magnetic film. (d) Decoupling parameter ΔR_y under the triaxial displacement of the magnetic film. (e) ALL sensor calibration using a motor drag rail. (f) Relationship between ΔR_y and the velocity of robotic fish of three ALL sensors.

the special magnetic field generated by the magnetic film, as shown in Fig. 2(b). Since the magnetic film and the Hall sensor are located on the exterior and interior sides of the robotic fish, respectively, their separation distance slightly varies depending on the installation position, and is approximately 20 mm.

As the robotic fish swims forward, water flows over the sensor surface, and the spatial displacement of the centripetally magnetized film can be calculated through the triaxial magnetic data measured by the 3D Hall sensor, thus reflecting the flow velocity, as shown in Fig. 2(c) and (d). The non-contact nature of magnetic field sensing enables segregated installation of sensor components, with electronic modules housed within the robotic fish's interior and deformable sensing elements positioned externally on the shell. As the water velocity increases, the displacement of the magnetic film will also increase, causing differences in magnetic field signals. Fig. 2(e) presents the fluid-structure interaction (FSI) simulation results obtained from COMSOL Multiphysics. As the flow velocity increases from 0 to 0.40 m/s, the displacement of the magnetic film rises from 0 to 3.78 mm. According to the simulation results, it can be seen that the displacement of the magnetic film has a quadratic relationship with flow velocity.

C. Performance of the Sensor

The magnetic film used in the ALL sensor has centripetal magnetization, as shown in Fig. 3(a) and (b) shows the actual magnetic field distribution of the magnetic film captured by a magneto-optic camera (MagView S, Matesy GmbH, Germany). Due to the special centripetal magnetization of the magnetic film, a 3D self-decoupling theory is proposed. Considering a planar structure, of thickness d, lying in the XY-plane. The upper and lower surface are at z = d and z = 0. The ideal centripetal magnetization arrangement of a magnetic film is assumed to be the superposition of two orthogonal sinusoidal curves in the x-y plane. Thus, the flux densities of the periodically centripetal magnetized film can be calculated in all three axes [22]:

$$B_x = -Ke^{kz}\sin(kx) \tag{1}$$

$$B_y = -Ke^{kz}\sin(ky) \tag{2}$$

$$B_z = Ke^{kz}\left(\cos(kx)+\cos(ky)\right) \tag{3}$$

Where B_x, B_y and B_z are the magnetic flux densities of the periodic centripetal magnetized film in the three axes, respectively. Therefore, the magnet's displacement Δx, Δy, Δz along three axis can be calculated:

$$\Delta x = x_1 - x_0 = \frac{1}{k}\Delta Rx = \frac{1}{k}\left(Rx(x_1,y_1,z_1) - Rx(x_0,y_0,z_0)\right) \tag{4}$$

$$\Delta y = y_1 - y_0 = \frac{1}{k}\Delta Ry = \frac{1}{k}\left(Ry(x_1,y_1,z_1) - Ry(x_0,y_0,z_0)\right) \tag{5}$$

$$\Delta z = z_1 - z_0 = \frac{1}{k}\Delta Sz = \frac{1}{k}\left(Sz(x_1,y_1,z_1) - Sz(x_0,y_0,z_0)\right) \tag{6}$$

where

$$Rx = \arctan\left(\frac{B_x}{B_z - \dfrac{B_z^2 - (B_y^2 - B_x^2)}{2B_z}}\right) \tag{7}$$

$$Ry = \arctan\left(\frac{B_y}{B_z - \dfrac{B_z^2 + (B_y^2 - B_x^2)}{2B_z}}\right) \tag{8}$$

$$S_z = \ln\left(\sqrt{\left(B_z - \frac{B_z^2 + (B_y^2 - B_x^2)}{2B_z}\right)^2 + B_y^2}\right) \quad (9)$$

R_x, R_y, S_z are the decoupling parameters. Thus, the magnetic film with ideal centripetal magnetization is theoretically proved to have 3-axis displacement decoupling ability.

It has to be pointed out that the above 3D self-decoupling model is derived from an ideal magnetic film with an infinite period area, and centripetal sinusoidal magnetization pattern, which is extremely challenging to achieve in practical experiments. But in previous work [21], it has been proven that the single-period folding magnetization method of the magnetic film in this experiment is consistent with the ideal magnetization method in terms of magnetic field distribution.

Taking Y as the forward direction of the robotic fish, and based on this 3D self-decoupling model, when the water flow generates shear displacement on the sensor surface, the decoupling parameter R_y can be calculated from the three-axis magnetic flux density signal obtained by the Hall sensor, thereby estimating the velocity of the robotic fish. To further illustrate the decoupling characteristics, Fig. 3(c) shows that the original magnetic field signal B_y not only changes with the displacement of the magnetic film in the Y direction, but is also affected by the displacement of the magnetic film in the X and Z directions. However, the decoupling parameter ΔR_y increases with the displacement of the magnetic film in the Y direction, but is unaffected by displacements in the X and Z directions, as shown in Fig. 3(d). To calibrate the ALL sensor, the robotic fish is dragged in a straight line for 3 meters in the water pool at different speeds using a motor drag rail, as shown in Fig. 3(e). Due to the decoupling ability of the ALL sensor, only ΔR_y needs to be recorded at different dragging speeds. By recording the three-axis magnetic field data of the three sensors over a certain period of time and calculating R_y, the relationship between ΔR_y and the velocity of fish can be obtained. Three fitting curves are then derived, as shown in Fig. 3(f), with coefficients of determination (R^2) of 0.9987, 0.9976 and 0.9968, respectively.

When the BCF-driven robotic fish swims forward, it generates yaw motion noise and pitch motion noise, as well as inevitable vortices interference around the ALL sensors, which results in displacements of the magnetic film in the X and Z directions. However, due to the 3D decoupling capability of the ALL sensors, these noise do not interfere with the R_y signal along the fish's forward direction, and thus do not affect the measurement of its forward swimming speed. To further illustrate the ALL sensor's performance of 3D decoupling, as shown in Fig. 4, in the 0-5s interval, the magnetic film on the robotic fish only has displacement in the Y direction, while in the 6-11s interval, the displacement of the magnetic film in the Y direction remains consistent with that in the 0-5s interval, but there is an additional irregular displacement in the X direction. It can be observed that the calculated decoupling parameter R_y in the 6-11s interval is essentially consistent with the one in the 0-5s interval, proving the effectiveness of the decoupling principle. In addition, we also compared velocity estimation results based on the coupled parameter By and found that using the decoupled parameter Ry can reduce the velocity estimation error by 43.42% (see Supporting Video).

From Fig. 3(f) it can be observed that as the velocity of fish increases, the error bars of the three sensors also increase.

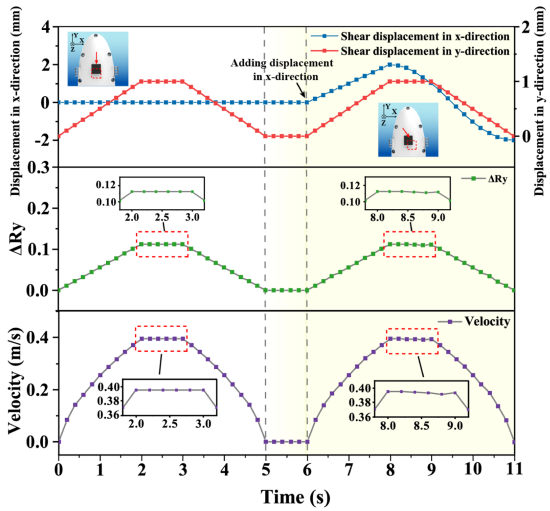

Fig. 4. The effect of the magnetic film displacement in the x-direction on the decoupling parameter ΔR_y and estimated velocity.

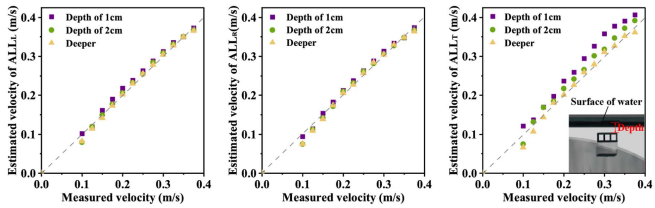

Fig. 5. The impact of the depth from the water surface on the velocity measurement accuracy of the three ALL sensors.

The average error bar of the three sensors at 0.1 m/s is 0.0054 m/s, while it increases to 0.0100 m/s at 0.3 m/s. This is likely due to the fact that, as the velocity of fish increases, the sensors experience greater disturbance from vortices, leading to increased interference. In addition, the error bar of the top sensor is significantly higher than that of the other two sensors. This is suspected to be due to interference from the viscous drag at the water surface bounda. Therefore, calibration experiments were conducted for the sensors of the robotic fish at different distances from the water surface, and the results are shown in Fig. 5. It indicates that at different distances from the water surface, the estimated velocity and measured velocity of ALL_L and ALL_R exhibit good consistency, while ALL_T shows significant variation, thereby confirming the proposed viewpoint. This indicates that the sensor's location on the robotic fish affects its sensing performance, with sensors mounted on the sides performing better than that mounted on the top.

III. Methods and Experiment

A. Experiment Setup

The experiments were carried out in a pool, whose size was 3.5 × 2.5 × 1.0 m, and the depth of the water was 0.7 m. A camera suspended above the pool is used to capture the motion video of the robotic fish and after subsequent path labeling, a 2D motion trajectory of the fish is obtained, as shown in Fig. 6(a). Though the trajectory of the robotic fish measured by the camera is in a 2D plane, it should be noted that the

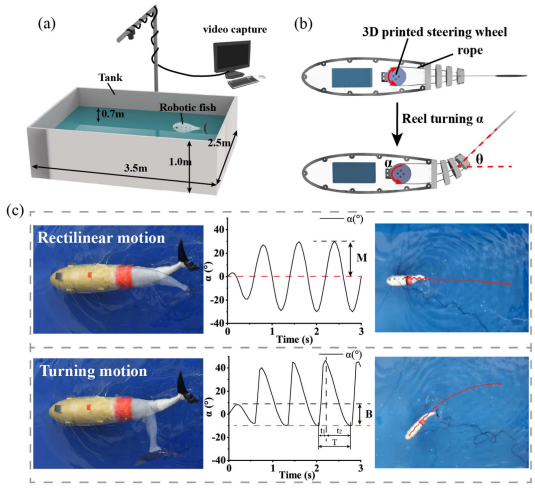

Fig. 6. Experimental environment and swimming principle of the robotic fish. (a) Experimental environment. (b) Illustration of the wire-driven mechanism of the robotic fish. (c) Two types of swimming motion of the robotic fish.

proposed trajectory prediction method can be fully used for 3D trajectory measurements without modification, due to the decoupling capability of the ALL sensor.

B. Swimming Motion of the Robotic Fish

The robotic fish used in the experiment adopts the BCF propulsion mode, whose flapping pattern is determined by the wire-driven mechanism and the compliant tail. As shown in Fig. 6(b), the robotic fish's tail has four joints, and assuming that the rotation angle of each joint is the same as the distance between each adjacent vertebra, the relationship between the rotation angle α of the servo motor and the bending angle ϕ of the tail can be expressed as [23]:

$$\Phi = 2N \sin^{-1}\left(\frac{\alpha r}{Nd}\right) \tag{10}$$

where d is the distance between the two wires, r is the radius of the reel. Thus, by changing the rotation angle α of the reel, the flapping angle ϕ of the robotic fish's tail can be adjusted, thereby enabling different swimming motions.

CPG is a bio-inspired controller that can generate coordinated oscillatory patterns of rhythmic activity [24]. The CPG control used in this letter is based on a open source model [23], [25], which has shown good performance on a wire-driven robotic fish. Different swimming modes of the robotic fish can be controlled by four parameters (M, ω, B, R). The model can be expressed as:

$$\ddot{b} = k_b(0.25k_b(B - b) - \dot{b}), \tag{11}$$

$$\ddot{m} = k_m(0.25k_m(M - m) - \dot{m}), \tag{12}$$

$$\dot{\phi} = \left[\frac{(1+R)^2}{4R} - \frac{R^2-1}{4R}\,\mathrm{sgn}(\sin\phi)\right]\omega, \tag{13}$$

$$\alpha = b + m\cos(\phi) \tag{14}$$

where b is the offset state, k_b is a positive constant, B is the high-level control command of the offset, m is the amplitude state, k_m is a positive constant, M is the high-level control command of amplitude, ϕ is the phase state, ω is the high-level control command of flapping frequency and α is the output of the CPG oscillator.

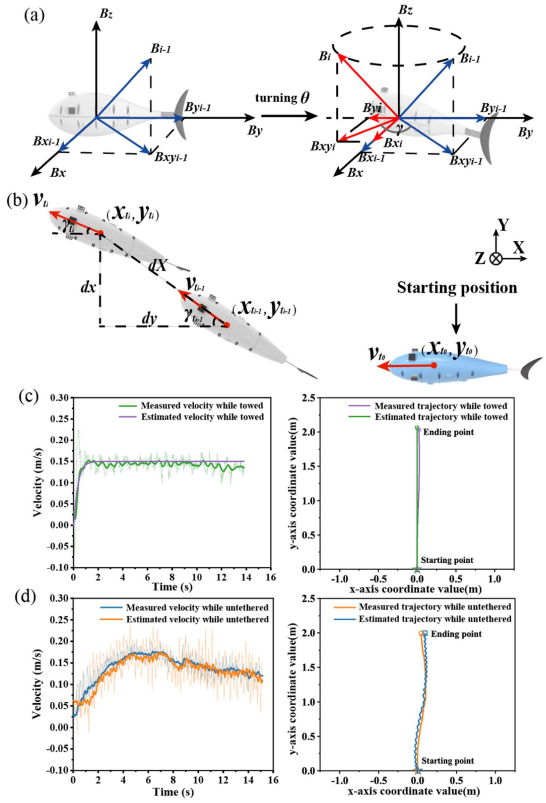

Fig. 7. Principle of trajectory estimation. (a) Illustration of the robotic fish calculating the steering angle by sensing the constant geomagnetic field in a small range. (b) Illustration of the trajectory estimation principal of the robotic fish. (c) Velocity and trajectory estimation results of the ALL array while the fish is towed. (d) Velocity and trajectory estimation results of the ALL array while the fish is untethered.

As shown in Fig. 6(c), based on the above CPG model, the robotic fish can achieve two types of motion modes: rectilinear motion and turning motion. For rectilinear motion, the left and right oscillation amplitudes of the robotic fish's tail are the same, meaning R=1 and the offset B=0, while for turning motion, the left and right oscillation amplitudes of the robotic fish's tail are different, which means the time ratio R is not equal to 1. To achieve smoother turning of the robotic fish and reduce large vibrations in its body, the value of B used in this experiment is slightly smaller than M. In the subsequent experiments, to enable real-time sensor data acquisition, a signal transmission line is connected from the top of the robotic fish to the PC side, without affecting the swimming performance of the fish.

C. Principle of Trajectory Estimation

When the robotic fish swims in a small area, its swimming direction can be directly obtained by an angle sensor, which works by calculating the 3D magnetic flux density of the environmental magnetic field (within a small region, the environmental magnetic field can be considered constant), as shown in Fig. 7(a). B_x-B_y-B_z is the magnetic field coordinate axes of the angle sensor. B_{i-1} is the environmental magnetic field with constant magnitude and direction at time t_{i-1}. B_{i-1XY} is the projection of the environmental magnetic field onto the XY-plane. When

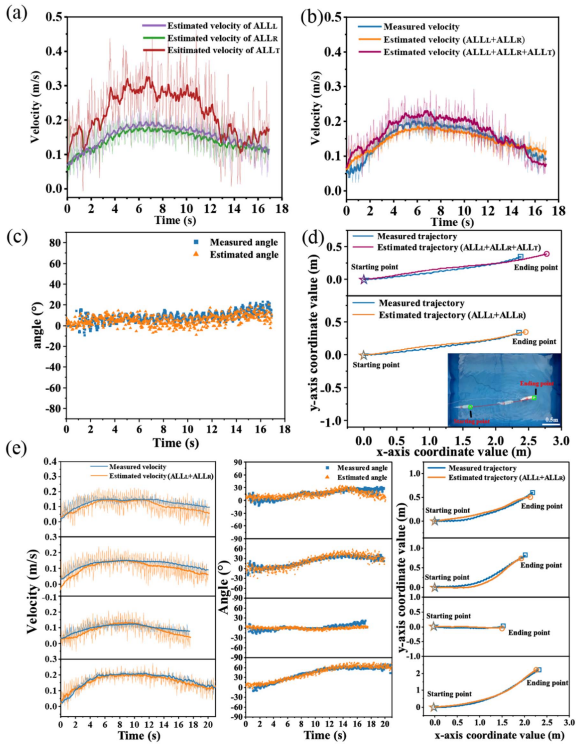

Fig. 8. Experiment results of rectilinear motion. (a) The estimated velocity of ALL_L, ALL_R and ALL_T. (b) The measured velocity and fused velocity of ALL_L + ALL_R and ALL_L + ALL_R + ALL_T. (c) The measured and estimated angle. (d) The measured trajectory and estimated trajectory of ALL_L + ALL_R and ALL_L + ALL_R + ALL_T. (e) Four more trials.

the swimming direction of the robotic fish rotates by θ, it can be considered as the environmental magnetic field B_0 rotating θ degrees in the opposite direction within the B_x-B_y-B_z coordinate system.

After steering θ, the environmental magnetic field and its projection onto the XY-plane are denoted as B_i and B_{ixy}, respectively. Therefore, the robotic fish's steering angle θ can be calculated as:

$$\theta = \arccos\left(\frac{B_{xi-1}B_{xi} + B_{yi-1}B_{yi}}{\sqrt{B_{xi-1}^2 + B_{yi-1}^2}\sqrt{B_{xi}^2 + B_{yi}^2}}\right) \times \cdot \frac{B_{xi-1}B_{yi} - B_{xi}B_{yi-1}}{|B_{xi-1}B_{yi} - B_{xi}B_{yi-1}|} \tag{15}$$

where B_{xi-1} and B_{yi-1} are the magnetic flux densities along the X and Y coordinates before the robotic fish steering measured by the sensor, respectively, and B_{xi} and B_{yi} are the magnetic flux densities along the X and Y coordinates after the robotic fish steering measured by the sensor, respectively.

By combining the steering angle estimated by the geomagnetic sensor and the forward velocity estimated by the ALL sensor array, the trajectory estimation of the robotic fish within a small region can be achieved, as shown in Fig. 7(b). In a still water environment, assuming the initial swimming time of the robotic fish is t_0, and the velocity detected by the ALL sensor array at time t is v_t, based on the principle of relative velocity, the robotic fish's own velocity at time t is also v_t. Therefore, the total distance traveled by the robotic fish in time t_i can be

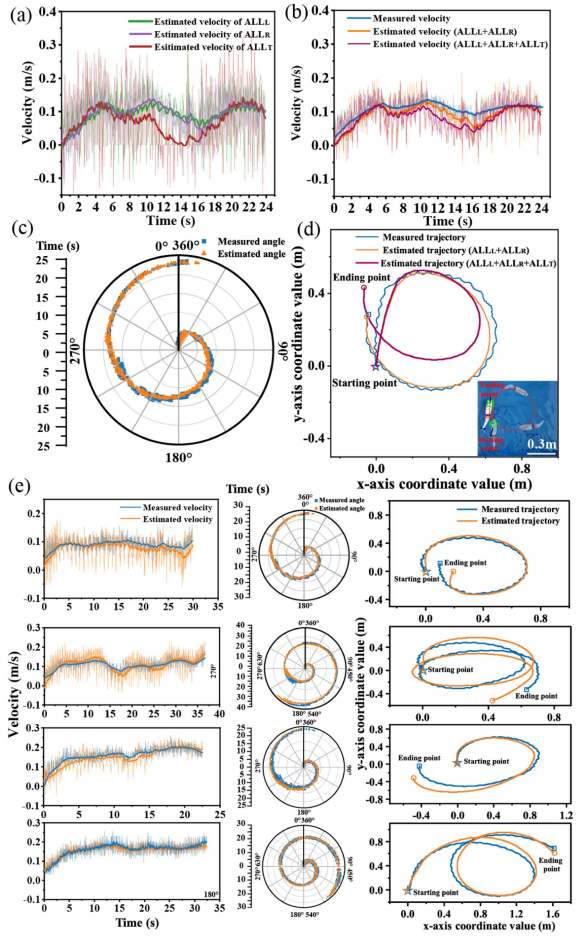

Fig. 9. Experiment results of turning motion. (a) The estimated velocity of ALL_L, ALL_R and ALL_T. (b) The measured velocity and fused velocity of ALL_L + ALL_R and ALL_L + ALL_R + ALL_T. (c) The measured and estimated angle. (d) The measured trajectory and estimated trajectory of ALL_L + ALL_R and ALL_L + ALL_R + ALL_T. (e) Four more trials.

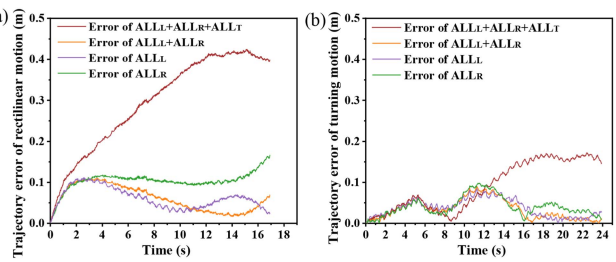

Fig. 10. Estimation error of two swimming motions. (a) MAE of rectilinear motion. (b) MAE of turning motion.

calculated as:

$$Xt_i = \int v_t dt \tag{16}$$

Thus, the displacement dX_i of the robotic fish during the time t_{i-1} and t_i interval can be expressed as:

$$dX_i = Xt_i - Xt_{i-1} \tag{17}$$

Assuming the robotic fish's moving angle relative to the origin at time t_i is θ_{t_i}, the coordinates of the robotic fish in the x-y

TABLE I
COMPARISON WITH EXISTING ALL SENSORS

ALL sensors	Akanyeti et al. [16]	Wang et al. [14]	Zheng et al. [9]	Zhang et al. [13]	Our work
Number of sensors	9	9	9	8	2
MAE of velocity in rectilinear	0.022 m/s	0.020 m/s	0.0060 m/s	0.016 m/s	0.015 m/s
MAE of velocity in turning	/	/	0.0052 m/s	0.011 m/s	0.013 m/s
MAE (Normalized MAE) of trajectory in rectilinear	/	/	>5.7%	0.12 m (∼ 1.2%)	0.060 m (2.6%)
MAE (Normalized MAE) of trajectory in turning	/	/	>8.0%	0.048 m (∼ 0.4%)	0.073 m (2.1%)
Whether the transient velocity is measurable	Yes	No	Yes	Yes	Yes
Experiment platform	Towed robotic fish	Robotic fish	Robotic fish	Robotic fish	Robotic fish
Types of sensor	Pressure-based	Pressure-based	Pressure-based	Deformation-based	Deformation-based

Considering accumulated error, the trajectory error is also represented as Normalized MAE, calculated by dividing MAE by the total path length.

plane can be expressed as:

$$x_{t_i} = x_{t_{i-1}} + \cos\theta_{t_i} \cdot dX_i \tag{18}$$

$$y_{t_i} = y_{t_{i-1}} + \sin\theta_{t_i} \cdot dX_i \tag{19}$$

where $x_{t_{i-1}}$, $y_{t_{i-1}}$ and x_{t_i}, y_{t_i} represent the coordinates of the robotic fish in the x-y plane at times t_{i-1} and t_i, respectively.

Since ALL_L and ALL_R are symmetrical in physical position to the center of the robotic fish, the output of the ALL array can be obtained by averaging the outputs of these two sensors. To compare the ALL's performance with and without the robotic fish's self-motion, the fish was towed along a 2-meter rail at a speed of 0.15 m/s and the results are shown in Fig. 7(c). It can be seen that due to the sudden start of the rail, the sensor signal exhibits significant fluctuation at the very initial moment and the mean absolute error (MAE) of velocity estimation is 0.0076 m/s after exponential smoothing. And the MAE of trajectory estimation is 0.0201 m. In contrast, the robotic fish is remotely controlled to swim freely along a straight path of approximately 2 meters and the results are shown in Fig. 7(d). It can be observed that while the fish is untethered, the overall trends of the measured velocity and estimated velocity still match well, with a MAE of 0.0095 m/s. And the MAE of trajectory estimation is 0.0302 m. This comparative experiment demonstrates that the self-motion noise of the robotic fish has minimal impact on the performance of the ALL array.

IV. RESULTS

A. Rectilinear Motion

For rectilinear motion, the robotic fish is remotely and manually controlled via a controller to swim freely in a straight line for 17 s in the pool, accelerating first and then decelerating. Fig. 8(a) shows the velocity estimated by ALL_L, ALL_R and ALL_T. It can be seen that the velocity estimated by ALL_T differs significantly from that of the other two side sensors and exhibits more pronounced fluctuations. Fig. 8(b) shows the comparison between the velocity measured by the camera, the fused velocity of ALL_L + ALL_R and the fused velocity of ALL_L + ALL_R + ALL_T. The results show that the estimated velocity of ALL_L + ALL_R has a linearity (R^2) of 0.9608, and the MAE is 0.0127 m/s, while the estimated velocity of ALL_L + ALL_R + ALL_T has a linearity (R^2) of only 0.8493, and the MAE is 0.0201 m/s. Meanwhile, compared with using ALL_L and ALL_R individually, the fusion of velocity data from both sensors can reduce velocity fluctuations to a certain extent, with variances of 0.00135, 0.00167 and 0.00108 m^2/s^2, respectively. Fig. 8(c) shows the measured and estimated swimming angle of rectilinear motion in 17s. The error in the angle estimation mainly arises from the possibility that the robotic fish may have a slight pitch angle while swimming, which causes changes in the projection of the environmental magnetic field onto the XY-plane. It should be pointed out that, due to the inherent drift in the angle sensor used to estimate the environmental magnetic field, calibration is required before each measurement to subtract this drift. Fig. 8(d) shows the comparison between the trajectory measured by the camera, the fused trajectory of ALL_L + ALL_R and the fused trajectory of ALL_L + ALL_R+ ALL_T. It can be observed that, compared to the fusion of all three sensors, the trajectory detected by fusing the two side sensors more closely matches the actual path. The trajectory error detected by ALL_L, ALL_R, ALL_L + ALL_R and ALL_L + ALL_R + ALL_T in rectilinear motion is shown in Fig. 10(a), whose MAEs are 0.0621 m, 0.1040 m, 0.0607 m and 0.2961 m, respectively, while the total path length is 2.48 m. The results show that the sensors mounted on the sides of the robotic fish demonstrate better velocity and trajectory detection performance than the top-mounted sensor. Moreover, the fused output from the two side sensors is more effective compared to using only a single sensor.

Additionally, the robotic fish was made to repeat the straight-line path for four more times, with results fusing the two side sensors shown in the Fig. 8(e). Based on all five trials, the MAE of velocity estimation and trajectory estimation in rectilinear motion is 0.0153 m/s and 0.0600 m, respectively, while the average total path length is 2.34 m.

B. Turning Motion

As for turning motion, the robotic fish was remotely and manually controlled to swim in circle freely in the pool for 23.9 s. Fig. 9(a) shows the velocity estimated by ALL_L, ALL_R and ALL_T in turning motion. Fig. 9(b) shows that the velocity measured by the camera and the fused velocity of ALL_L + ALL_R agree well, with a linearity (R^2) of 0.9138 and the MAE is 0.0148 m/s, while the estimated velocity of ALL_L + ALL_R + ALL_T has a linearity (R^2) of only 0.6643 and the MAE is 0.0224 m/s. The measured and estimated swimming angles of turning motion are shown in Fig. 9(c), and they show good agreement. The comparison between the trajectory measured by the camera, the fused trajectory of ALL_L + ALL_R and the fused trajectory of ALL_L + ALL_R + ALL_T in turning motion are shown in Fig. 9(d), which similarly indicates that the top sensor introduces greater errors. The trajectory error detected by ALL_L, ALL_R, ALL_L + ALL_R and ALL_L + ALL_R + ALL_T in turning motion is shown in Fig. 10(b), whose MAEs are 0.0375 m, 0.0414 m, 0.0344 m and 0.0915 m, respectively, while the total path length is 2.27 m. The results demonstrate that in turning motion, fusing the two side sensors also provides more accurate results than including the top sensor or relying on only single sensor.

Similarly, the robotic fish was made to repeat the turning motion for four more times, with results fusing the two side sensors shown in the Fig. 9(e). Based on all five trials, the MAE of velocity estimation and trajectory estimation in turning motion is 0.0125 m/s and 0.0730 m, respectively, while the average total path length is 3.50 m. More information including field experiment is shown in Supporting Video.

V. Conclusion

In this work, we propose a magnetic ALL sensor that can detect the flow velocity by sensing the displacement of the magnetic film as the water flows over. The proposed ALL sensor has three-dimensional decoupling flow velocity sensing capability, allowing it to remain unaffected by the self-motion noise of the robotic fish as well as the turbulence interference in non-velocity directions. Through theoretical analysis, multiphysics simulation, and experiments, the effectiveness of the ALL's flow velocity-decoupling sensing capability is demonstrated. An ALL array was designed and mounted on both sides of a robotic fish, enabling it to perceive its swimming velocity with fused data. Based on this capability, the demonstration of the ALL sensor in robotic fish's trajectory esitimation is vertified under both rectilinear and turning motion. The experimental results show that the MAE of velocity estimation in rectilinear and turning motions is 0.0153 m/s and 0.0125 m/s, respectively. And the MAE of trajectory estimation in rectilinear and turning motion is 0.0600 m and 0.0730 m, respectively, while the distances traveled by the robotic fish are 2.34 m and 3.50 m. The performance comparison between our method and the existing ALL sensors is shown in Table I, which shows that our approach can significantly reduce the number of ALL sensors required while achieving both accurate velocity and trajectory estimation on an untethered robotic fish.

Future work involves using the ALL array to perceive the complex three-dimensional motion of robotic fish in a wild environment with random flow. In addition, combining data from the ALL array with that from sensors such as the IMU to further improve the accuracy of estimation, in order to achieve closed-loop control of the robotic fish's speed, is also a direction worth exploring in the future. Furthermore, we hope to use the ALL sensor array to explore more applications for robotic fish, such as obstacle avoidance, automatic trajectory correction, and so on.

References

[1] X. Irigoien, J. Huisman, and R. P. Harris, "Global biodiversity patterns of marine phytoplankton and zooplankton," *Nature*, vol. 429, no. 6994, pp. 863–867, 2004.

[2] J. Qu et al., "Recent advances on underwater soft robots," *Adv. Intell. Syst.*, vol. 6, no. 2, 2024, Art. no. 2300299.

[3] S. Heshmati-Alamdari, A. Nikou, and D. V. Dimarogonas, "Robust trajectory tracking control for underactuated autonomous underwater vehicles in uncertain environments," *IEEE Trans. Autom. Sci. Eng.*, vol. 18, no. 3, pp. 1288–1301, Jul. 2021.

[4] S. Dai, Z. Wu, S. Li, J. Wang, M. Tan, and J. Yu, "Model-based event-triggered dynamic pursuing and surrounding control for a multi-robotic fish system," *IEEE Robot. Automat. Lett.*, vol. 8, no. 6, pp. 3788–3795, Jun. 2023.

[5] J. Han et al., "Data-assisted dynamic modeling of bionic robotic fish and its precise speed control," *IEEE Robot. Automat. Lett.*, vol. 9, no. 11, pp. 10447–10454, Nov. 2024.

[6] Y. Zhang et al., "A manta ray-inspired fast-swimming soft electrohydraulic robotic fish," *IEEE Robot. Automat. Lett.*, vol. 9, no. 9, pp. 8043–8050, Sep. 2024.

[7] R. K. Katzschmann, J. DelPreto, R. MacCurdy, and D. Rus, "Exploration of underwater life with an acoustically controlled soft robotic fish," *Sci. Robot.*, vol. 3, no. 16, 2018, Art. no. eaar3449.

[8] Z. Wu, J. Liu, J. Yu, and H. Fang, "Development of a novel robotic dolphin and its application to water quality monitoring," *IEEE/ASME Trans. Mechatron.*, vol. 22, no. 5, pp. 2130–2140, Oct. 2017.

[9] X. Zheng, W. Wang, M. Xiong, and G. Xie, "Online state estimation of a fin-actuated underwater robot using artificial lateral line system," *IEEE Trans. Robot.*, vol. 36, no. 2, pp. 472–487, Apr. 2020.

[10] Z. Wang, S. Wang, and X. Luo, "Underwater surface flow velocity sensor based on single side stray field of permanent magnet," *IEEE Trans. Instrum. Meas.*, vol. 72, 2023, Art. no. 7504215.

[11] J. C. Montgomery, C. F. Baker, and A. G. Carton, "The lateral line can mediate rheotaxis in fish," *Nature*, vol. 389, no. 6654, pp. 960–963, 1997.

[12] T. Shizhe, "Underwater artificial lateral line flow sensors," *Microsystem Technol.*, vol. 20, pp. 2123–2136, 2014.

[13] Z. Zhang, C. Zhou, L. Cheng, X. Wang, and M. Tan, "Real-time velocity vector resolving of artificial lateral line array with fishlike motion noise suppression," *IEEE Trans. Robot.*, vol. 39, no. 6, pp. 4350–4365, Dec. 2023.

[14] W. Wang, Y. Li, X. Zhang, C. Wang, S. Chen, and G. Xie, "Speed evaluation of a freely swimming robotic fish with an artificial lateral line," in *Proc. 2016 IEEE Int. Conf. Robot. Automat.*, 2016, pp. 4737–4742.

[15] Y. Xu and K. Mohseni, "Fish lateral line inspired hydrodynamic force estimation for autonomous underwater vehicle control," in *Proc. 52nd IEEE Conf. Decis. Control*, 2013, pp. 6156–6161.

[16] O. Akanyeti et al., "Self-motion effects on hydrodynamic pressure sensing: Part I. Forward–backward motion," *Bioinspiration Biomimetics*, vol. 8, no. 2, 2013, Art. no. 026001.

[17] J. Fu, Y. Jiang, and D. Zhang, "PVDF based artificial canal lateral line for underwater detection," in *Proc. 2015 IEEE Sensors*, 2015, pp. 1–4.

[18] H. Hans, J. Miao, P. V. Y. Alvarado, and M. S. Triantafyllou, "Chemical composition and physical features of harbor seal (Phoca Vitulina) vibrissae for underwater sensing application," in *Proc. 2011 IEEE Int. Conf. Robot. Biomimetics*, 2011, pp. 1439–1443.

[19] H. Bleckmann and R. Zelick, "Lateral line system of fish," *Integrative Zool.*, vol. 4, no. 1, pp. 13–25, 2009.

[20] Y. Zhai, X. Zheng, and G. Xie, "Fish lateral line inspired flow sensors and flow-aided control: A review," *J. Bionic Eng.*, vol. 18, pp. 264–291, 2021.

[21] H. Dai et al., "Split-type magnetic soft tactile sensor with 3D force decoupling," *Adv. Mater.*, vol. 36, no. 11, 2024, Art. no. 2310145.

[22] J. Mallinson, "One-sided fluxes–A magnetic curiosity?," *IEEE Trans. Magn.*, vol. 9, no. 4, pp. 678–682, Dec. 1973.

[23] F. Xie, Y. Zhong, R. Du, and Z. Li, "Central pattern generator (CPG) control of a biomimetic robot fish for multimodal swimming," *J. Bionic Eng.*, vol. 16, pp. 222–234, 2019.

[24] A. J. Ijspeert, "Central pattern generators for locomotion control in animals and robots: A review," *Neural Netw.*, vol. 21, no. 4, pp. 642–653, 2008.

[25] A. J. Ijspeert, A. Crespi, D. Ryczko, and J.-M. Cabelguen, "From swimming to walking with a salamander robot driven by a spinal cord model," *Science*, vol. 315, no. 5817, pp. 1416–1420, 2007.